Computer Modeling in Engineering & Sciences
DOI:10.32604/cmes.2020.09898
Article

T-Splines for Isogeometric Analysis of Two-Dimensional Nonlinear Problems

Mayi Guo, Gang Zhao, Wei Wang*, Xiaoxiao Du, Ran Zhang and Jiaming Yang

School of Mechanical Engineering and Automation, Beihang University, Beijing, 100191, China
*Corresponding Author: Wei Wang. Email: jrrt@buaa.edu.cn
Received: 25 January 2020; Accepted: 24 February 2020

Abstract: Nonlinear behaviors are commonplace in many complex engineering applications, e.g., metal forming, vehicle crash test and so on. This paper focuses on the T-spline based isogeometric analysis of two-dimensional nonlinear problems including general large deformation hyperelastic problems and small deformation elastoplastic problems, to reveal the advantages of local refinement property of T-splines in describing nonlinear behavior of materials. By applying the adaptive refinement capability of T-splines during the iteration process of analysis, the numerical simulation accuracy of the nonlinear model could be increased dramatically. The Bézier extraction of the T-splines provides an element structure for isogeometric analysis that can be easily incorporated into existing nonlinear finite element codes. In addition, T-splines show great superiority of modeling complex geometries especially when the model is irregular and with hole features. Several numerical examples have been tested to validate the accuracy and convergence of the proposed method. The obtained results are compared with those from NURBS-based isogeometric analysis and commercial software ABAQUS.

Keywords: Isogeometric analysis; T-splines; nonlinear; hyperelasticity; elastoplasticity; adaptive refinement

1 Introduction

Isogeometric analysis (IGA), introduced by Cottrell et al. [1], employs the same basis functions in geometry representation and analysis. The reuse of the geometric model in the analysis process saves a lot of time for manual interactions to construct the analysis-suitable mesh, especially when the geometry needs to be modified. Due to the exact geometry representation, high-order continuity, and high accuracy, IGA offers significant advantages over FEA and is being expected to be implemented in CAE software as well as exert its full potentials in industry practices.

IGA has been successfully applied to many engineering problems including shape optimization [2–6], topological optimization [7–13], contact problem [14,15], fluid [16–18], fracture and damage [19–22]. Besides, the applications of IGA also include the interpretation of nonlinear material and nonlinear geometric problems such as elastoplastic material, nearly incompressible material and large deformation behavior [23–29]. In [23], IGA can accurately describe the large plastic deformation and calculate accurate results. It is worth mentioning that, the high-order NURBS basis functions based IGA can

greatly alleviate the phenomenon of self-locking, which is generally an unavoidable problem in low-order finite element method.

Although IGA owns many advantages, a variety of the CAD models represented by NURBS cannot be directly used in the analysis [30–32]. The tensor-product topological structure of NURBS limits its ability to represent a complex model by using one single patch. When modeling complicated products in practical industry scenarios, thousands of tensor product NURBS patches may be used to comprise the special shape features needed by the design. Trimming curves are used to cut out the original defined NURBS patches and then piece them together to achieve arbitrary topologies, so gaps and overlaps will be produced unavoidably. Another defect of NURBS is that the local refinement cannot be defined within it because it is based on a tensor-product mesh which means the control points should be aligned on a rectangular grid regularly. Due to these reasons, the NURBS-based global discretization, is usually not suitable as a basis for isogeometric analysis. As a generalization of NURBS, T-splines were introduced in the CAD community, which were formulated to overcome the main drawbacks of NURBS mentioned above [33]. Generally, the trimmed model based on NURBS could be represented by an untrimmed T-spline and the model using multiple patches could be merged into one single, watertight T-spline [34]. Furthermore, for the sake of the accuracy of the numerical simulation, adaptive refinement has been actively explored within the framework of isogeometric analysis [35–38]. Different from NURBS, local refinement can be achieved in T-splines [39] without propagating superfluous control points when implementing the knot insertion algorithm. These superiorities make T-splines a powerful technology for geometric discretization as well as the integration of design-through analysis applications [40–42].

In this work, we use T-splines as a basis to perform analysis of complex nonlinear models, including hyperelasticity and elastoplasticity material models. We use T-splines to model designs traditionally with trimming features as one single, watertight geometry, which makes the integration of design and analysis for two-dimensional models more seamless and efficient. Moreover, we combine the error estimate with the local refinement capabilities of T-splines. Starting from a coarse uniform NURBS mesh, our approach performs the adaptive refinement of the T-mesh during the iteration process of nonlinear analysis. The adaptive T-spline meshes possess similar convergence properties to uniform meshes with fewer degrees-of-freedom (Dofs).

The paper is outlined as follows: In Section 2 we give a brief review of T-splines and Bézier extraction. The main formulations about hyperelastic materials and elastoplastic materials are given in Section 3. The error estimate and adaptive strategy are presented in Section 4. In Section 5, we consider some examples of trimmed models and compare adaptive refinement T-spline meshes with uniform meshes in the two-dimensional nonlinear problem. The conclusions and directions for future research are discussed in Section 6.

2 T-splines and Bézier Extraction

NURBS has been widely used in the field of CAD due to its superior mathematical and algorithmic properties. The NURBS basis functions own some preferable properties such as the partition of unity, non-negativity and linear independence. However, it is severely limited by its tensor product topological structure. The T-spline surface is a non-uniform B-spline surface with T-junctions which help T-splines to model the complex design as one single watertight geometry and achieve local refinement. In this section, we present a brief overview of fundamental T-spline concepts. More details are presented in [33].

2.1 The T-spline Basis

A T-spline surface is constructed from a T-mesh. For surfaces, the T-mesh is a mesh of two-dimensional polygonal elements. A T-mesh in the index space is shown in Fig. 1a. A major difference between a T-mesh and a NURBS mesh is the existence of T-junctions, which are analogous to hanging nodes in the conventional

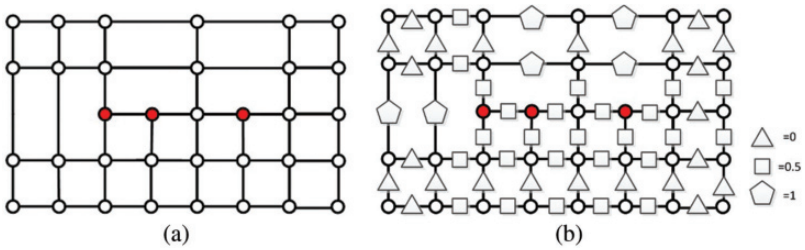

Figure 1: (a) Example of T-mesh in the index space. (b) Knot interval configuration of the T-mesh

finite element. (see the red circles in Fig. 1a). To define T-spline parametric information and basis functions, knot intervals (non-negative real numbers) should be specified for the T-mesh. An effective knot interval configuration demands that the knot interval of each side equal to that of the opposite. As shown in Fig. 1b, the triangles, squares, and pentagons correspond to knot intervals of 0, 0.5 and 1, respectively.

A T-spline surface is defined by a T-mesh with valid knot interval configuration and T-spline basis functions constructed from the configuration. The equation of a T-spline surface is as:

$$T(u,v) = \sum_{i=0}^{n} P_i R_i(u,v), (u,v) \in \Omega \tag{1}$$

where each control point P_i, is associated with a weight w_i, and a blending function $R_i(u,v)$ is given by:

$$R_i(u,v) = \frac{w_i N_i^k(u) N_i^l(v)}{\sum_{j=0}^{n} w_j N_j^k(u) N_j^l(v)}. \tag{2}$$

$N_i^k(u)$ and $N_i^l(v)$ are the B-spline basis functions corresponding to the control point P_i with k degree in u-direction and l degree in v-direction. A cubic T-spline mesh is shown in Fig. 2. $N_1^3(u)$ and $N_1^3(v)$ are cubic B-spline basis functions corresponding to the control point P_1, which are defined over the horizontal knots [u_1, u_2, u_3, u_4, u_5] and the vertical knots [v_1, v_2, v_3, v_4, v_5]. In our research, we choose cubic T-splines as the basis for nonlinear isogeometric analysis, without losing generality.

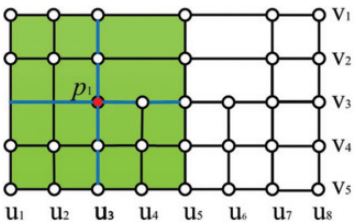

Figure 2: The parameter domain corresponding to the control point P_1

2.2 Bézier Extraction of T-Splines

The Bézier extraction of T-splines is important for analysis because it delimits elements where T-spline basis functions are guaranteed to be C^∞. Thus, these delimited elements are called Bézier elements. The Bézier extraction operation provides an element structure for isogeometric analysis which can be easily incorporated into existing finite element codes. The details of Bézier extraction are presented in [43,44].

In a certain element e, the T-spline basis functions $N^e(\xi)$ can be represented by a linear combination of the Bernstein polynomial basis $B^e(\xi)$ through the Bézier extraction. The T-spline basis function $N^e(\xi)$ can be expressed as:

$$N^e(\xi) = C^e B^e(\xi) \tag{3}$$

where C^e is called the element Bézier extraction operator, which is based on knot insertion. ξ is the coordinate in the parent element domain.

The a^{th} rational T-spline basis function $R_a^e(\xi)$ over the element e can be written as:

$$R_a^e(\xi) = \frac{w_a^e N_a^e(\xi)}{\sum_{j=0}^{n} w_j^e N_j^e(\xi)} \tag{4}$$

where w_j^e represents the weight of the control point which is corresponding to the j^{th} T-spline basis function over the element e. Given a set of T-splines control points P_i^e of the element e, the element geometric map x^e from the parent element domain to the physical space can be defined as:

$$x^e(\xi) = \sum_{i=0}^{n} P_i^e R_i^e(\xi). \tag{5}$$

3 Nonlinear Formulations

The formulations of nonlinear isogeometric analysis in our work are summarized in this section. For two-dimensional hyperelastic problems, the large deformation, large stress and large strain are studied and for two-dimensional elastoplasticity problems, only the small deformation case is considered at this stage. Readers are referred to [45–49] for more details of the formulation.

3.1 Hyperelasticity

In the displacement-based implementation of isogeometric analysis, the $\mathbf{u}_i$ is the displacement of control points. The displacement can be calculated by the following scheme:

$$\mathbf{u} = \sum_{i=0}^{n} R_i(\xi, \eta)\mathbf{u}_i \tag{6}$$

where $R_i(\xi, \eta)$ is the basis function for isogeometric analysis. The reference coordinate $\mathbf{X}$ is expressed by the nodal coordinate in the undeformed geometry as:

$$\mathbf{X} = \sum_{i=0}^{n} R_i(\xi, \eta)\mathbf{X}_i. \tag{7}$$

Then, the displacement gradient is given by:

$$\nabla_0 \mathbf{u} = \frac{\partial \mathbf{u}}{\partial \mathbf{X}} = \sum_{i=0}^{n} \frac{\partial R_i(\xi, \eta)}{\partial \mathbf{X}} \mathbf{u}_i. \tag{8}$$

The deformation gradient is defined by:

$$\mathbf{F} = 1 + \nabla_0 \mathbf{u}, \tag{9}$$

and the Lagrangian strain $\mathbf{E}$ is written as:

$$\mathbf{E} = \frac{1}{2}(\mathbf{F}^{\mathrm{T}}\mathbf{F} - 1). \tag{10}$$

Next, the variation of the Lagrangian strain is given by:

$$\bar{\mathbf{E}} = \mathbf{B}_N \bar{\mathbf{u}} \tag{11}$$

where $\mathbf{B}_N$ is the nonlinear displacement-strain matrix, which contains the components of the deformation gradient and $\bar{\mathbf{u}}$ is the variation of nodal displacements. The discrete energy form is obtained by using Eq. (11) and the second Piola-Kirchhoff stress $\mathbf{S}$ as:

$$a(\mathbf{u}, \bar{\mathbf{u}}) = \int_{\Omega} \mathbf{S} : \bar{\mathbf{E}} d\Omega \equiv \bar{\mathbf{u}}^{\mathrm{T}} \mathbf{f}^{\mathrm{int}} \tag{12}$$

where $\mathbf{f}^{\mathrm{int}}$ is the discrete internal force vector. Furthermore, the discrete version of external force vector is written as:

$$l(\bar{\mathbf{u}}) = \int_{\Omega} \bar{\mathbf{u}} \cdot \mathbf{f}_b d\Omega + \int_{\Gamma_N} \bar{\mathbf{u}} \cdot \hat{\mathbf{t}} d\Gamma \equiv \bar{\mathbf{u}}^{\mathrm{T}} \mathbf{f}^{ext} \tag{13}$$

where $\mathbf{f}_b$ and $\hat{\mathbf{t}}$ denote the body force and prescribed traction. The nonlinear equation is solved by finding the internal force which is equal to the external force:

$$\bar{\mathbf{u}}^{\mathrm{T}} \mathbf{f}^{\mathrm{int}}(\mathbf{u}) = \bar{\mathbf{u}}^{\mathrm{T}} \mathbf{f}^{ext}. \tag{14}$$

The solution of Eq. (14) requires an iterative method, such as the modified Newton-Raphson method, which needs the tangent stiffness matrix.

The incremental Lagrangian strain can be calculated as:

$$\Delta \mathbf{E} = \mathbf{B}_N \Delta \mathbf{u}. \tag{15}$$

The first term of the structural energy form is expressed as:

$$\int_{\Omega} \bar{\mathbf{E}} : \mathbf{D}_N : \Delta \mathbf{E} d\Omega = \bar{\mathbf{u}}^{\mathrm{T}} \left[\int_{\Omega} \mathbf{B}_N^{\mathrm{T}} \mathbf{D}_N \mathbf{B}_N d\Omega \right] \Delta \mathbf{u}. \tag{16}$$

Then, the second term in the linearized energy form is expressed as:

$$\int_{\Omega} \mathbf{S} : \Delta \bar{\mathbf{E}} d\Omega = \bar{\mathbf{u}}^{\mathrm{T}} \left[\int_{\Omega} \mathbf{B}_G^{\mathrm{T}} \Sigma \mathbf{B}_G d\Omega \right] \Delta \mathbf{u} \tag{17}$$

where

$$\Sigma = \begin{bmatrix} S_{11} & S_{12} & 0 & 0 \\ S_{12} & S_{22} & 0 & 0 \\ 0 & 0 & S_{11} & S_{12} \\ 0 & 0 & S_{12} & S_{22} \end{bmatrix}, \tag{18}$$

$$\mathbf{B}_G = \begin{bmatrix} R_{0,1} & 0 & R_{1,1} & 0 & \dots & R_{n,1} & 0 \\ R_{0,2} & 0 & R_{1,2} & 0 & \dots & R_{n,2} & 0 \\ 0 & R_{0,1} & 0 & R_{1,1} & \dots & 0 & R_{n,1} \\ 0 & R_{0,2} & 0 & R_{1,2} & \dots & 0 & R_{n,2} \end{bmatrix}. \tag{19}$$

$R_{i,j}$ denote the derivative of $R_i(\xi, \eta)$ with respect to the reference configuration $\mathbf{X}$ in the j^{th} direction. The tangent stiffness matrix is derived by Eqs. (16) and (17) as:

$$\mathbf{K}_T = \int_{\Omega} (\mathbf{B}_N^{\mathrm{T}} \mathbf{D}_N \mathbf{B}_N + \mathbf{B}_G^{\mathrm{T}} \Sigma \mathbf{B}_G) d\Omega. \tag{20}$$

The discretized version of incremental equation can now be written as:

$$\bar{\mathbf{u}}^{\mathrm{T}} \mathbf{K}_T \Delta \mathbf{u} = \bar{\mathbf{u}}^{\mathrm{T}} (\mathbf{f}^{ext} - \mathbf{f}^{\mathrm{int}}). \tag{21}$$

Iterative methods, such as the modified Newton-Raphson method, can be employed to solve the above system of equations until the residual force on the right is equal to zero. If the incremental force method is applied, the Newton-Raphson method will be used at each load step.

3.2 Elastoplasticity

For elastoplasticity, the stress does not have a one-to-one relationship with the strain. At each integration point of the element, the plastic variables and the stress are calculated by the past load history and the return-mapping algorithm. In the return-mapping algorithm, the elastic trial status is computed first, assuming that all strain increments are elastic. The trial stress $\boldsymbol{\eta}^{tr}$ at the n^{th} load step can be written as:

$$\eta^{tr} = {}^{n}\mathbf{s} + 2\mu\Delta\mathbf{e} - {}^{n}\boldsymbol{\alpha} \tag{22}$$

where $\mathbf{s}$ denotes the stress deviator; μ means the shear modulus; $\mathbf{e}$ is the deviatoric strain, and $\boldsymbol{\alpha}$ states the back stress denoting the shifted vector of the yield surface due to the kinematic hardening. Assume that von Mises yield criterion and the combined hardening criterion are used, the yield function is expressed as:

$$f = \|\eta^{tr}\| - \sqrt{\frac{3}{2}}\left[\sigma_Y^0 + (1-\beta) H e_p\right]. \tag{23}$$

σ_Y^0 and H are initial yield stress and plastic modulus; e_p denotes the effective plastic strain; the parameter $\beta \in [0, 1]$ states the influence of the isotropic hardening and kinematic hardening in the combined hardening. If $f \leq 0$, the material status is elastic. Then, the trail predictors are performed to update the plastic variables and the stress:

$${}^{n+1}\mathbf{s} = {}^{n}\mathbf{s} + 2\mu\Delta\mathbf{e}, {}^{n+1}\boldsymbol{\alpha} = {}^{n}\boldsymbol{\alpha}, {}^{n+1}e_p = {}^{n}e_p. \tag{24}$$

If $f > 0$, the material status has become plastic. What's more, the plastic correction step should be performed to find the plastic status, as follows:

$${}^{n+1}\mathbf{s} = {}^{tr}\mathbf{s} - 2\mu\Delta\boldsymbol{\varepsilon}^p = {}^{tr}\mathbf{s} - 2\mu\hat{\gamma}\mathbf{N} \tag{25}$$

where $\hat{\gamma} = f/\left(2\mu + \frac{2}{3}H\right)$ is the plastic consistency parameter, and $\mathbf{N} = {}^{tr}\boldsymbol{\eta}/\|{}^{tr}\boldsymbol{\eta}\|$ is a unit deviatoric tensor. The stress is updated as:

$${}^{n+1}\boldsymbol{\sigma} = {}^{n}\boldsymbol{\sigma} + \Delta\boldsymbol{\sigma} \tag{26}$$

where the increment of stress is obtained as:

$$\Delta\boldsymbol{\sigma} = \mathbf{D} : \Delta\varepsilon - 2\mu\hat{\gamma}\mathbf{N}. \tag{27}$$

According to the flow law, the plastic variables are updated together with the stress as:

$${}^{n+1}\alpha = {}^{n}\alpha + \frac{2}{3}\beta H\hat{\gamma}\mathbf{N}, \tag{28}$$

$${}^{n+1}e_p = {}^{n}e_p + \sqrt{\frac{2}{3}}\hat{\gamma}. \tag{29}$$

Assuming that the combined hardening is linear, from Eq. (27) the consistent or algorithmic tangent stiffness becomes:

$$\mathbf{D}^{ep} = \frac{\partial \Delta\sigma}{\partial \Delta\varepsilon} = \mathbf{D} - 2\mu\mathbf{N} \otimes \frac{\partial \hat{\gamma}}{\partial \Delta\varepsilon} - 2\mu\hat{\gamma}\frac{\partial \mathbf{N}}{\partial \Delta\varepsilon}. \tag{30}$$

The derivative of $\hat{\gamma}$ with respect to $\Delta\varepsilon$ is expressed as:

$$\frac{\partial \hat{\gamma}}{\partial \Delta\varepsilon} = \frac{2\mu\mathbf{N} \otimes \mathbf{N}}{2\mu + \frac{2}{3}H}. \tag{31}$$

The unit normal tensor increment is obtained as:

$$\frac{\partial \mathbf{N}}{\partial \Delta\varepsilon} = \frac{\partial \mathbf{N}}{\partial {}^{tr}\boldsymbol{\eta}} : \frac{\partial {}^{tr}\boldsymbol{\eta}}{\partial \Delta\varepsilon} = \left[\frac{\mathbf{I}}{\|{}^{tr}\boldsymbol{\eta}\|} - \frac{{}^{tr}\boldsymbol{\eta} \otimes {}^{tr}\boldsymbol{\eta}}{\|{}^{tr}\boldsymbol{\eta}\|^3}\right] : 2\mu\mathbf{I}_{dev} = \frac{2\mu}{\|{}^{tr}\boldsymbol{\eta}\|}\left[\mathbf{I}_{dev} - \mathbf{N} \otimes \mathbf{N}\right]. \tag{32}$$

$\mathbf{I}$ is the fourth-order unit symmetric tensor. $\mathbf{I}_{dev}$ is the fourth-order unit deviatoric tensor defined as $\mathbf{I}_{dev} = \mathbf{I} - \frac{1}{3}\mathbf{I} \otimes \mathbf{I}$. Thus, $\mathbf{D}_{ep}$ can be calculated as:

$$\mathbf{D}_{ep} = \frac{\partial \Delta\boldsymbol{\sigma}}{\partial \Delta\varepsilon} = \mathbf{D} - \frac{4\mu^2\mathbf{N} \otimes \mathbf{N}}{2\mu + \frac{2}{3}H} - \frac{4\mu^2\hat{\gamma}}{\|{}^{tr}\eta\|}\left[\mathbf{I}_{dev} - \mathbf{N} \otimes \mathbf{N}\right]. \tag{33}$$

The tangent stiffness matrix is calculated as:

$$\mathbf{K}_T = \int_\Omega \mathbf{B}^{\mathrm{T}}\mathbf{D}_{ep}\mathbf{B}d\Omega \tag{34}$$

where $\mathbf{B}$ is the strain-displacement matrix. The discretized version of incremental equation is expressed as:

$$\bar{\mathbf{u}}^{\mathrm{T}}\mathbf{K}_T\Delta\mathbf{u} = \bar{\mathbf{u}}^{\mathrm{T}}(\mathbf{f}^{ext} - \mathbf{f}^{\mathrm{int}}). \tag{35}$$

Because ${}^{n+1}e_p$, ${}^{n+1}\boldsymbol{\alpha}$ and ${}^{n+1}\boldsymbol{\sigma}$ will be used in the next load step, the iteration process needs one more step to update them after the nonlinear equation converges.

3.3 Framework of Two-Dimensional Nonlinear Analysis

Although the previous sections summarized the steps of the nonlinear isogeometric analysis, it is also important to explain how these steps are performed sequentially. The flowchart of a nonlinear isogeometric analysis program is as shown in Fig. 3. In our work, we use the modified Newton-Raphson method and the incremental force method. When the Newton-Raphson method fails to converge, the bisection method will be used to control the load increment.

4 The Error Estimate and Adaptive Strategy

In our work, we apply the h-adaptive refinement strategy for two-dimensional nonlinear problems [50]. The h-adaptive strategy is used to improve the accuracy of nonlinear isogeometric analysis by refining the mesh during the iteration process while keeping the order of the basis function unchanged. Three main steps are involved in adaptive refinement:

1. Determine a reasonably accurate error estimator.
2. Perform the adaptive refinement to get the new mesh according to the estimate error.
3. Apply the second step cyclically until the estimate error is less than the prescribed value.

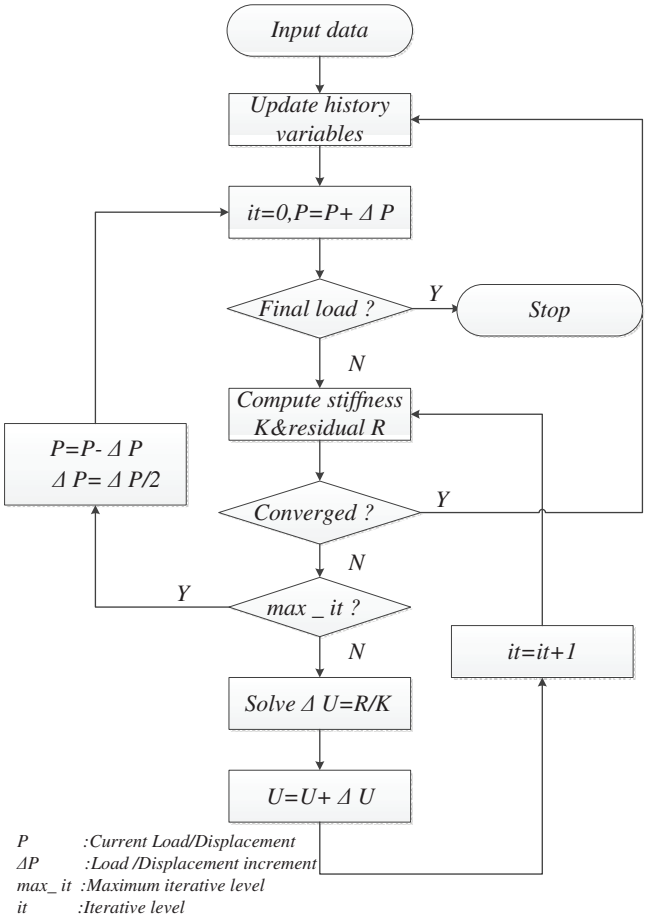

Figure 3: Flowchart for nonlinear isogeometric analysis procedure

All adaptive strategies are according to the fact that any calculation results obtained by initial numerical simulation will always produce a certain error. For the generation of a better mesh, the error should be estimated by an error estimator [51]. One such reasonably accurate error estimator and adaptive procedure, introduced by Zienkiewicz et al. [52], have been applied in many engineering fields as, for example, fluid, dynamic problems, and non-linear material models [53–55].

We obtain the approximate solution of stress $\hat{\boldsymbol{\sigma}}$ by a standard Galerkin process in the isogeometric analysis program. To obtain acceptable results for stresses, the projection process is generally used in which it is assumed that the stress is interpolated by the same function $\mathbf{R}$ as the displacement, i.e.,

$$\boldsymbol{\sigma}^* = \mathbf{R}\bar{\boldsymbol{\sigma}}^* \tag{36}$$

and

$$\int_{\Omega} \mathbf{R}^{\mathrm{T}}(\boldsymbol{\sigma}^* - \hat{\boldsymbol{\sigma}})d\Omega = 0. \tag{37}$$

On substitution of Eqs. (36) and (37) this yields:

$$\bar{\sigma}^* = \mathbf{A}^{-1} \int_{\Omega} \mathbf{R}^{\mathbf{T}} \hat{\sigma} d\Omega \tag{38}$$

where

$$\mathbf{A} = \int_{\Omega} \mathbf{R}^{\mathbf{T}} \mathbf{R} d\Omega. \tag{39}$$

It has been proved that $\boldsymbol{\sigma}$ * is in fact a better approximation than $\hat{\boldsymbol{\sigma}}$. Thus, the estimate error can be calculated as:

$$\mathbf{e}_{\sigma} = \boldsymbol{\sigma}^* - \hat{\boldsymbol{\sigma}}. \tag{40}$$

For the stresses the L_2 norm of the error $\mathbf{e}_{\boldsymbol{\sigma}}$ is

$$\|\mathbf{e}_{\boldsymbol{\sigma}}\| = (\int_{\Omega} (\mathbf{e}_{\boldsymbol{\sigma}})^{\mathbf{T}} (\mathbf{e}_{\boldsymbol{\sigma}}) d\Omega)^{1/2}. \tag{41}$$

The estimate for the local error of the i^{th} element is defined as $\|\mathbf{e}_{\boldsymbol{\sigma}}\|_i$. Thus, the global error is:

$$\|\mathbf{e}_{\boldsymbol{\sigma}}\| = (\sum_{i=1}^{nel} \|\mathbf{e}_{\boldsymbol{\sigma}}\|_i^2)^{1/2} \tag{42}$$

where *nel* is the total number of elements.

The relative error can be defined by:

$$\eta = \frac{\|\mathbf{e}_{\boldsymbol{\sigma}}\|}{\|\boldsymbol{\sigma}^*\|} \times 100\%. \tag{43}$$

The refinement strategy is decided by the error level that we wish to achieve. So, we require to keep η within the limit:

$$\eta \leq \bar{\eta} \tag{44}$$

where $\bar{\eta}$ is a prescribed error tolerance. If the error norm is under the tolerance, the solution is accepted and the iteration process proceeds to the next load step, keeping the mesh constant. If the error norm exceeds the limit, the mesh is refined and the current step is recalculated. As the local error $\|\mathbf{e}_{\boldsymbol{\sigma}}\|_i$ is in fact computed for each element we can conveniently check where local refinement is necessary. Let ξ_i denote the local refinement parameter, which is calculated by:

$$\xi_i = \frac{\|\mathbf{e}_{\boldsymbol{\sigma}}\|_i}{e_m}, \tag{45}$$

where e_m is the average error, i.e.,

$$e_m = \frac{\|\mathbf{e}_{\boldsymbol{\sigma}}\|}{\sqrt{nel}}. \tag{46}$$

During the adaptive refinement process, an element is refined or not according to the local refinement parameter. In implementation, the element of which this parameter is larger than 1 ($\xi_i > 1$) will be refined, as shown in Fig. 4. The details of the refinement of the T-mesh are presented in [33,39].

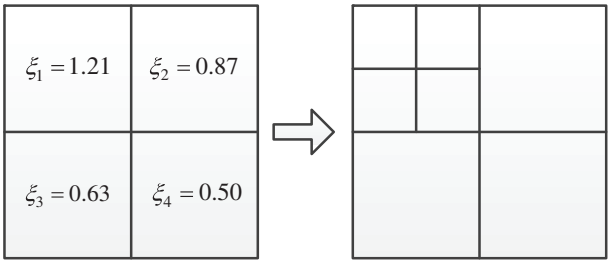

Figure 4: Mesh refinement according to the local refinement parameter

5 Numerical Examples

In this section, several examples are provided to explain the major advantages that T-splines bring to two-dimensional nonlinear isogeometric analysis. In the first part, two models with hole features or irregular boundaries are represented by untrimmed T-splines, which can be directly used in the isogeometric analysis. If the same model is represented by NURBS, more than ten patches need to be merged, as shown in Figs. 5d and 10d. In the second part, we compare the global refinement with the

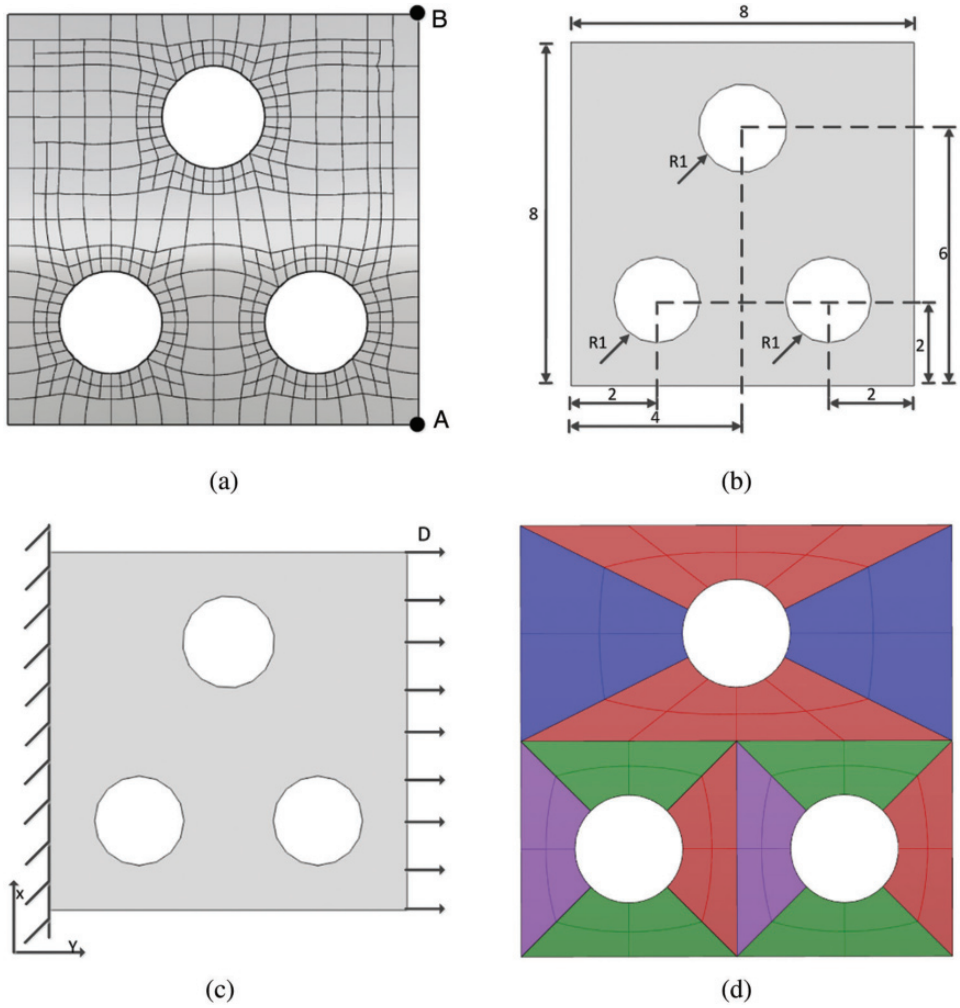

Figure 5: (a) T-spline surface of a square with three holes (b) The geometry size of the model (c) Boundary conditions of the model (d) The model of multiple NURBS patches merging

adaptive refinement to illustrate that the local refinement capabilities of T-splines enhance the accuracy of two-dimensional nonlinear problems, by two widespread examples.

5.1 Untrimmed T-splines in Two-Dimensional Nonlinear Analysis

A complicated engineering design represented by trimmed NURBS usually requires the pre-process before analysis. If we represent the model by a single untrimmed T-spline using the commercial software Rhino with the T-splines plugin, it can be directly applied in isogeometric analysis. The results calculated by T-spline IGA are compared with those from FEA(ABAQUS) to confirm the robustness and accuracy of T-splines in the nonlinear calculation. It is well known that the results of FEA will gradually converge with the refinement of the mesh, especially for the nonlinear problems. Thus, we adjust the approximate global size in the ABAQUS to refine the mesh until the change of the calculation results is within 1%. For the fairness of the comparison, the same strategy is also used for T-spline IGA to get acceptable results.

In the first example, the stretching of a square with three holes is investigated. Mooney-Rivlin hyperelastic material is used for this model with A10 = 0.1863, A01 = 0.00979, and K = 0. Geometry size of the model is shown in Fig. 5b. As shown in Fig. 5c, the left edge of the square is fixed, while the right edge is subjected to a prescribed x-displacement D = 8.

The distributions of von Mises stress and displacements are compared between T-spline IGA and the FEA (ABAQUS) in this example, as shown in Figs. 6–8. We also choose two points, A and B (Fig. 5a), to show the load-displacement curves, which is another important result to be studied. The load D is divided into 10 load steps equally for the comparison of our load-displacement curves with the results from the FEA, as shown in Fig. 9. The IGA uses a mesh with 1838 Dofs (or 500 elements based on Bézier extraction of T-splines), while a mesh with 20060 Dofs (or 6516 CPS8R elements) of the FEA is used. As the figures show, our simulation results agree well with those from FEA. As usual, the FEA uses rather more Dofs (or elements) to achieve the acceptable results. In contrast, our nonlinear IGA program using T-splines offers almost the same results with a lower number of Dofs. Generally speaking, this is known as the main advantage of the IGA method, no matter using T-splines or NURBS.

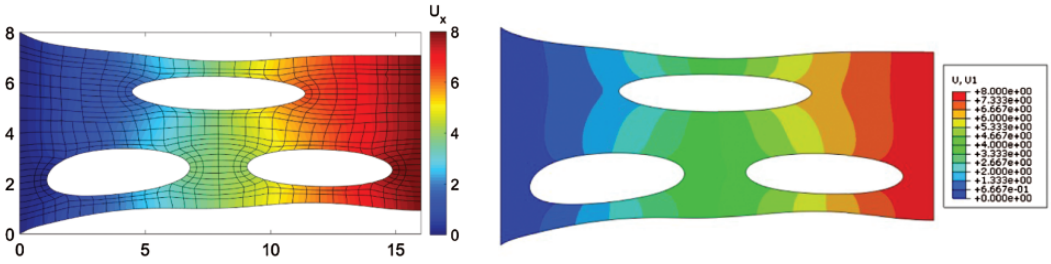

Figure 6: The distributions of the x-displacement of hyperelastic model (a) The T-spline IGA (b) The FEA (ABAQUS)

The second example is a trimmed elastoplastic square with two holes under a prescribed displacement, as shown in Fig. 10. Young's modulus E = 200 × 10e9, Poisson ratio $\nu = 0.29$, initial yield stress $Y_0 = 200 \times$ 10e6, plastic modulus H = 2.222 × 10e10, and isotropic hardening model is used. The geometry size of the model is as shown in Fig. 10b. For the boundary conditions: the x-displacement of the left edge is fixed, the y-displacements of the top edge and bottom edge are fixed, and the right edge is subjected to a prescribed x-displacement D = 0.008. A mesh with 1838 Dofs (or 478 elements) is used for IGA using T-splines, while a mesh with 12865 Dofs (or 4170 CPE8R elements) for the FEA. Similar to the previous example, the von

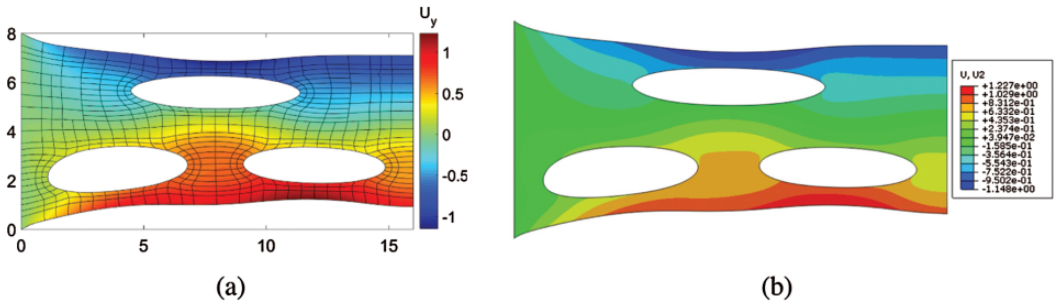

Figure 7: The distributions of the y-displacement of hyperelastic model (a) The T-spline IGA (b) The FEA (ABAQUS)

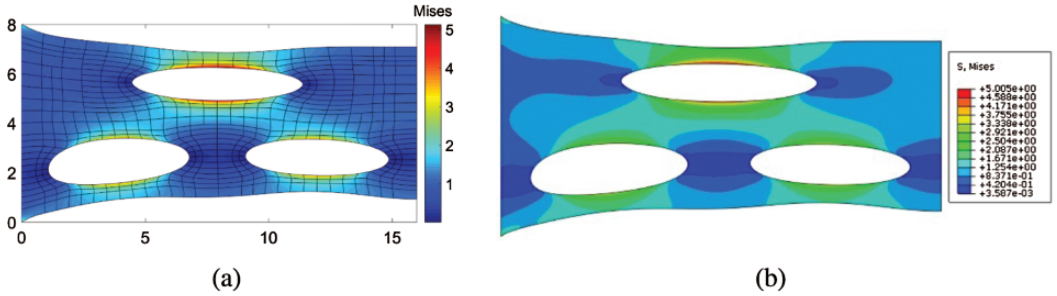

Figure 8: The distributions of the von Mises stress of hyperelastic model (a) The T-spline IGA (b) The FEA (ABAQUS)

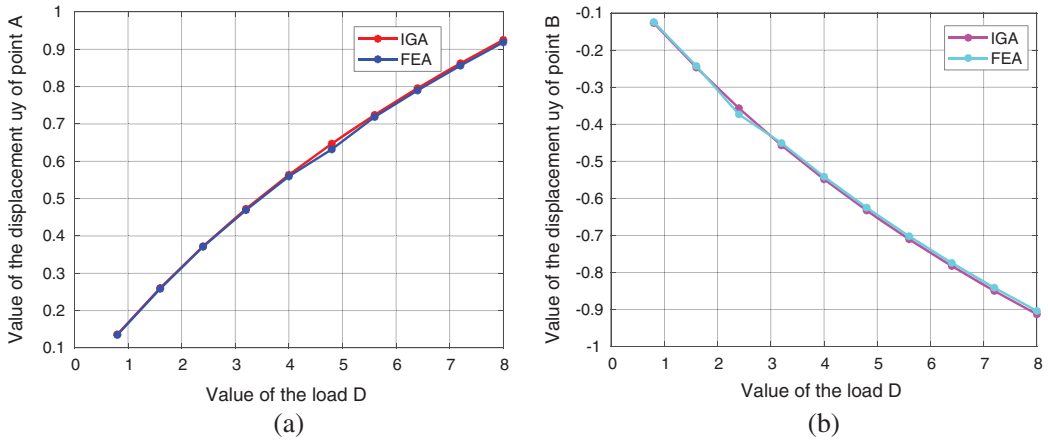

Figure 9: Comparison of the load-displacement curve between the IGA and FEA of hyperelastic model (a) The y-displacement of the point A (b) The y-displacement of the point B

Mises stress and the displacements computed by the T-spline based IGA are compared with those from the FEA, as shown in Figs. 11–13.

Moreover, the plastic regions are studied. The plastic regions calculated by the FEA (ABAQUS) compared with those derived from our proposed IGA based on T-splines are shown in Fig. 14. Obviously, the plastic regions calculated by the IGA is essentially the same as those from ABAQUS. Fig. 15 shows

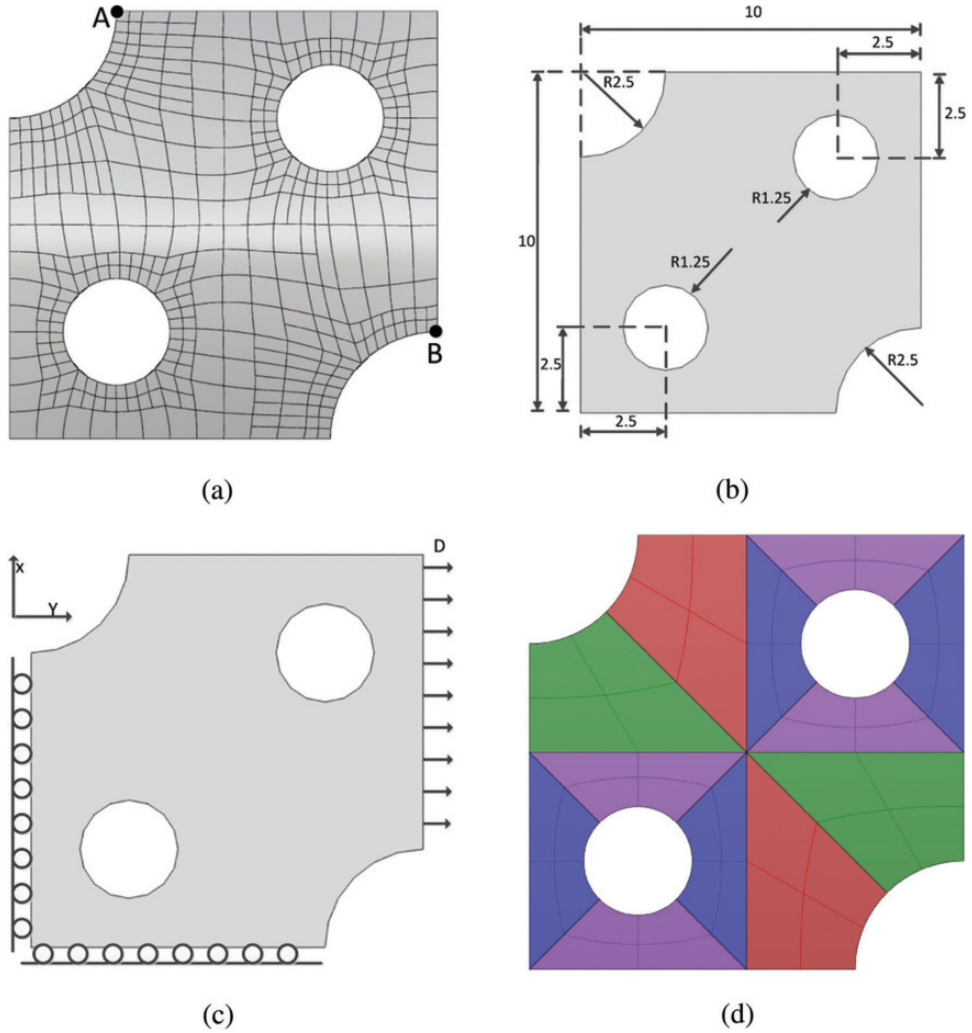

Figure 10: (a) T-spline surface of a trimmed square with two holes (b) The geometry size of the model (c) Boundary conditions of the model (d) The model of multiple NURBS patches merging

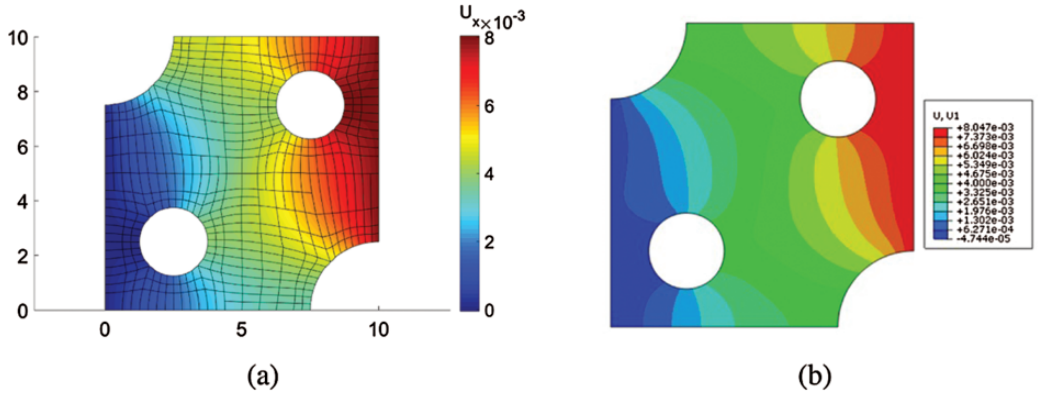

Figure 11: The distributions of the x-displacement of elastoplastic model (a) The T-spline IGA (b) The FEA (ABAQUS)

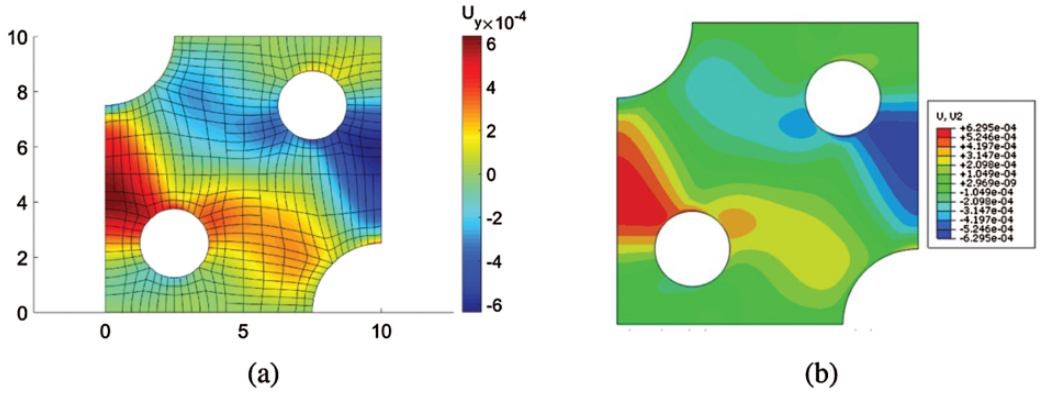

Figure 12: The distributions of the y-displacement of elastoplastic model (a) The T-spline IGA (b) The FEA (ABAQUS)

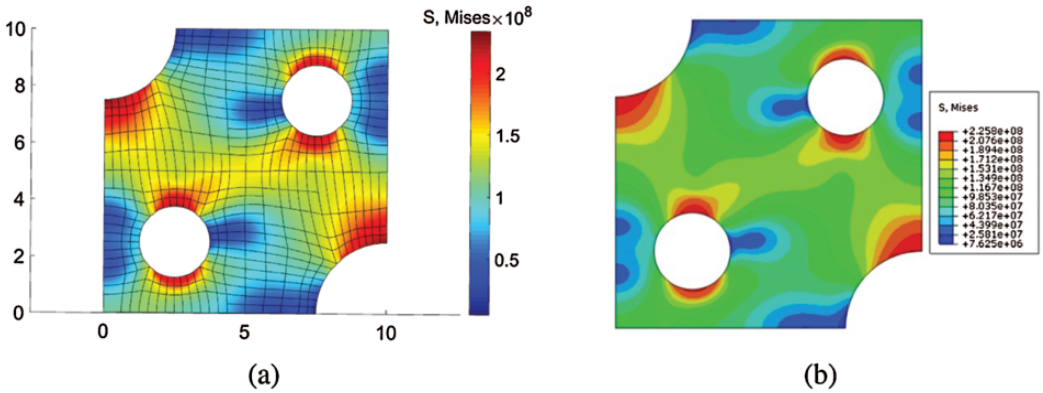

Figure 13: The distributions of the von Mises stress of elastoplastic model (a) The T-spline IGA (b) The FEA (ABAQUS)

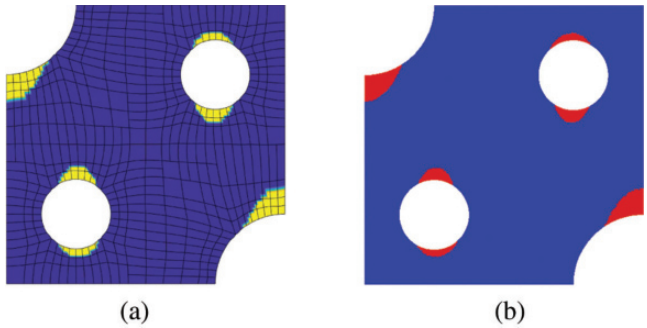

Figure 14: Comparison of the plastic regions (a) The T-spline IGA(yellow) (b) The FEA(red)

the load-displacement curves of the points A and B (Fig. 10a). Our curves have a good match with the results obtained by the FEA. In addition, because the point A is in the elastic region and the point B is in the plastic region, we can clearly see the strong nonlinearities due to the influence of plasticity.

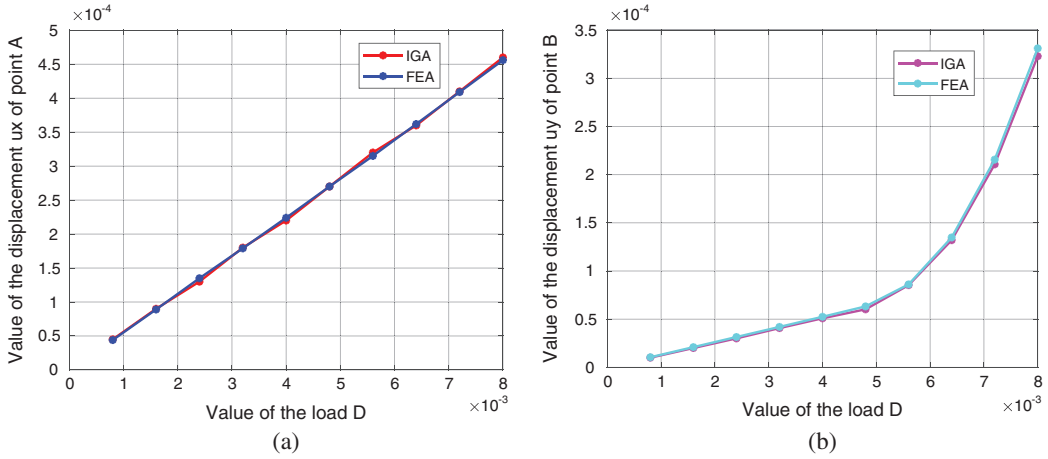

Figure 15: Comparison of the load-displacement curve between the IGA and FEA of elastoplastic model (a) The x-displacement of the point A (b) The y-displacement of the point B

5.2 Adaptive Refinement of T-Splines in Two-Dimensional Nonlinear Analysis

In this part, we provide two two-dimensional nonlinear common examples to illustrate that the adaptive T-spline meshes enhance the accuracy of per Dof compared with the global refinement. The first example deals with a one-quarter annular plate under small deformation whose geometry is schematically depicted in Fig. 16a. The inner radius r = 1, while the outer radius R = 2. The left edge fixed and the right edge is subjected to a prescribed y-displacement D = 0.008. For the material model: Young's modulus E = 200 × 10e9, Poisson ratio v = 0.29, initial yield stress Y_0 = 200 × 10e6, plastic modulus H = 2.222 × 10e10, and isotropic hardening model is used.

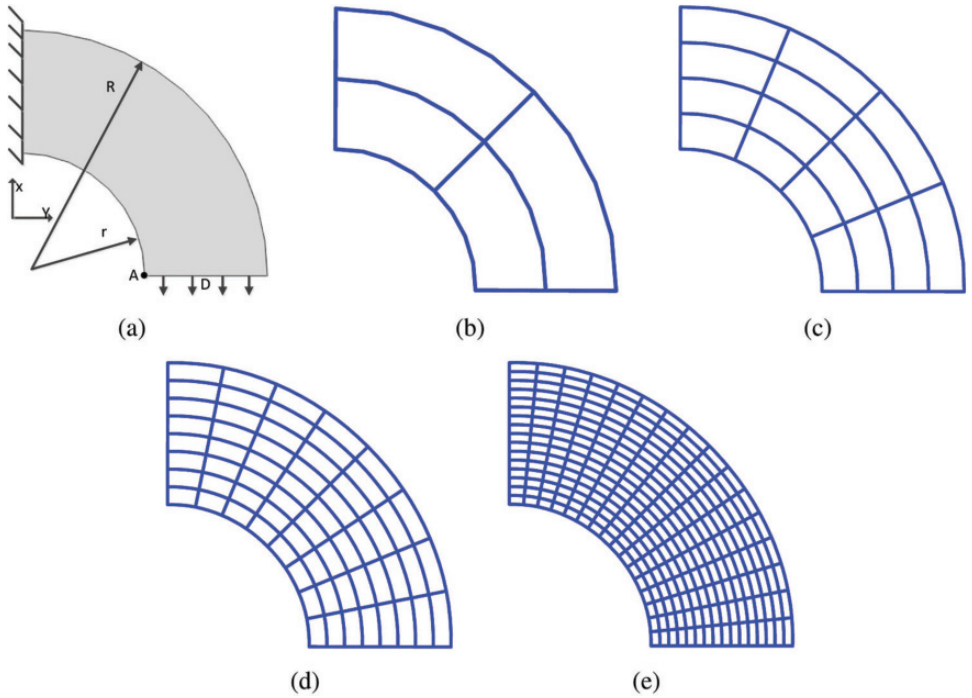

Figure 16: (a) Geometry size and boundary conditions of the model (b) The initial mesh 0 Dofs = 50 the relative error η = 40% (c) The mesh 1 Dofs = 98 η = 30% (d) The mesh 2 Dofs = 242 η = 25% (e) The mesh 3 Dofs = 722 η = 15%

Firstly, the global refinement meshes are investigated, as shown in Fig. 16. The mesh 0, mesh 1, mesh 2 and mesh 3, are performed in nonlinear IGA program, respectively. Thus, we get the relative errors approximately equal to 40%, 30%, 25%, and 15%. Then, the adaptive refinement analyses are also performed from the initial mesh 0. The corresponding meshes calculated from the nonlinear isogeometric analysis program are shown in Fig. 17, with prescribed relative errors 30%, 25%, and 15%. It is obvious that at the same error levels, the adaptive refinement processes bring a reduction of more than 20% in the number of Dofs. The computation results of the displacement ux of the point A and the number of Dofs during the adaptive analysis process are shown in Figs. 18 and 19.

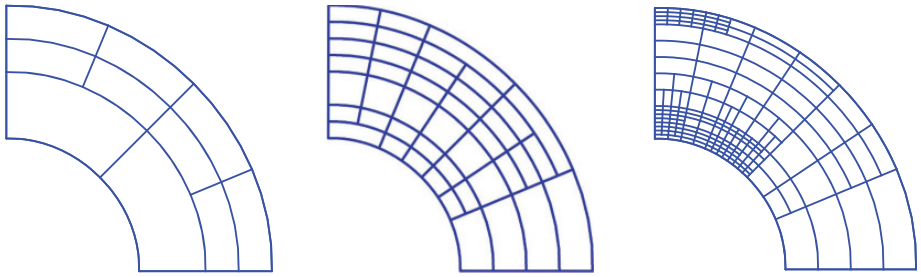

Figure 17: (a) The t-mesh 1 Dofs = 76 the prescribed error $\bar{\eta}$ = 30% (b) The t-mesh 2 Dofs = 176 the prescribed error $\bar{\eta}$ = 25% (c) The t-mesh 3 Dofs = 544 the prescribed error $\bar{\eta}$ = 15%

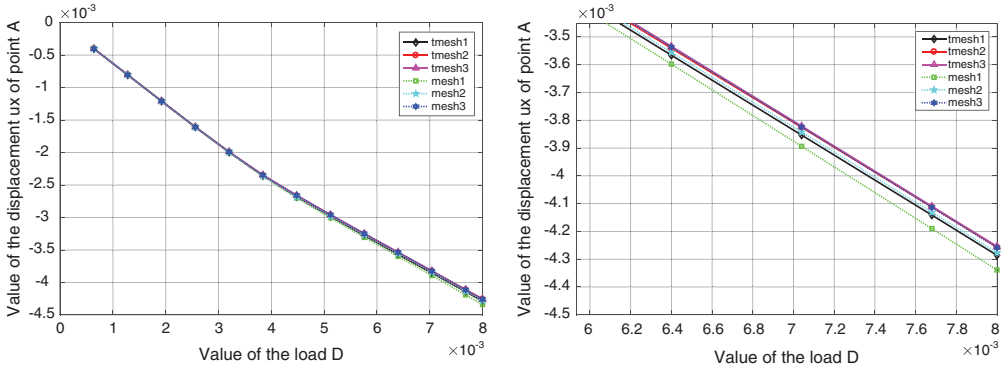

Figure 18: (a) The load-displacement curves of different meshes (b) A partial magnification of the load-displacement curves

The load-displacement curves of the point A (see Fig. 16a) is shown as the Fig. 18. For all meshes, with the refinement of the mesh, the displacements calculated by isogeometric analysis converge to the same results. Besides that, the Fig. 18b shows that the adaptive t-mesh with 176 Dofs (t-mesh 2) and the uniform mesh with 722 Dofs (mesh 3) seem to get the same results. It is clear that the adaptive refinement achieves similar precision with fewer Dofs compared with the global refinement. In this example we also study the convergence behavior of the displacement ux at point A. We choose the calculation result of the uniform mesh with 8978 Dofs as the exact result u_x^{exact}. Fig. 20 shows the absolute error $u_x - u_x^{exact}$, where u_x is the actual result achieved by the adaptive and the non-adaptive

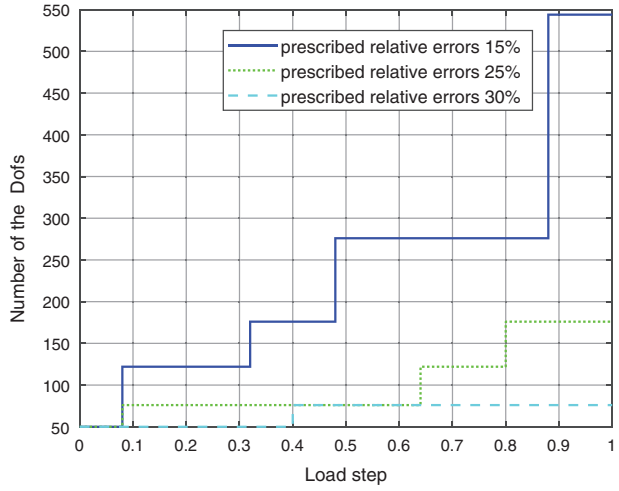

Figure 19: Number of Dofs given by the adaptive analysis

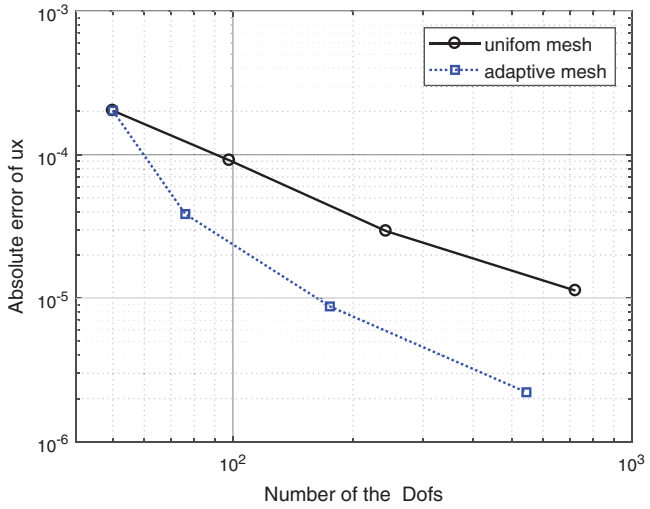

Figure 20: The error of the displacement u_x at point A

isogeometric analysis respectively. It can be seen again that the adaptive refinement has a better accuracy and convergence than the global refinement.

The second example is a hyperelastic model to illustrate the advantage of adaptive refinement in the accuracy of nonlinear analysis. In this example, the stretching of a unit square is investigated. As shown in Fig. 21, the left edge of the square is fixed, while the bottom edge simply supported. The right edge is subjected to a prescribed displacements D, which is five times its length, namely D = 5. Mooney-Rivlin hyperelastic material is used for this model with A10 = 0.1863, A01 = 0.00979, and K = 0.

For the global refinement, the relative errors approximately equal to 5.5%, 4.5%, 3.0%, and 1.5% are given by mesh 0, mesh 1, mesh 2 and mesh 3 in Fig. 22, respectively. If we choose prescribed relative errors as 4.5%, 3.0%, and 1.5%, we can get the corresponding adaptive meshes calculated from the nonlinear isogeometric analysis program, as shown in Fig. 23. Compared with the global refinement

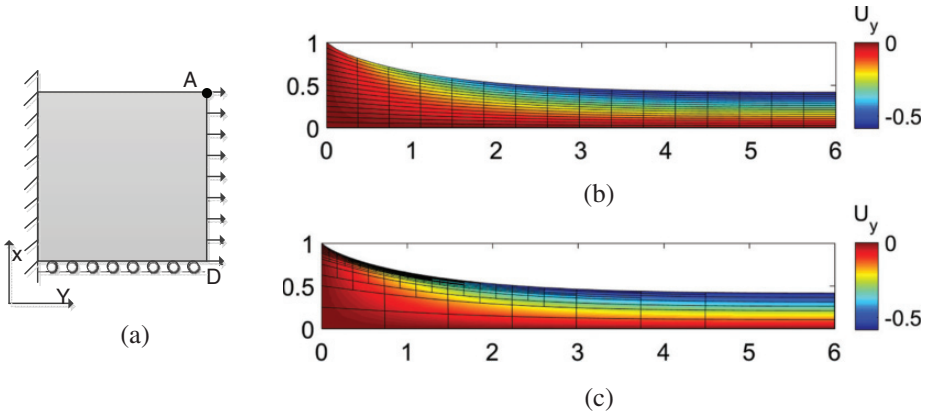

Figure 21: (a) Geometry size and boundary conditions of the model (b) The distribution of the y-displacement of the computation result (uniform mesh) (c) The distribution of the y-displacement of the computation result (adaptive mesh)

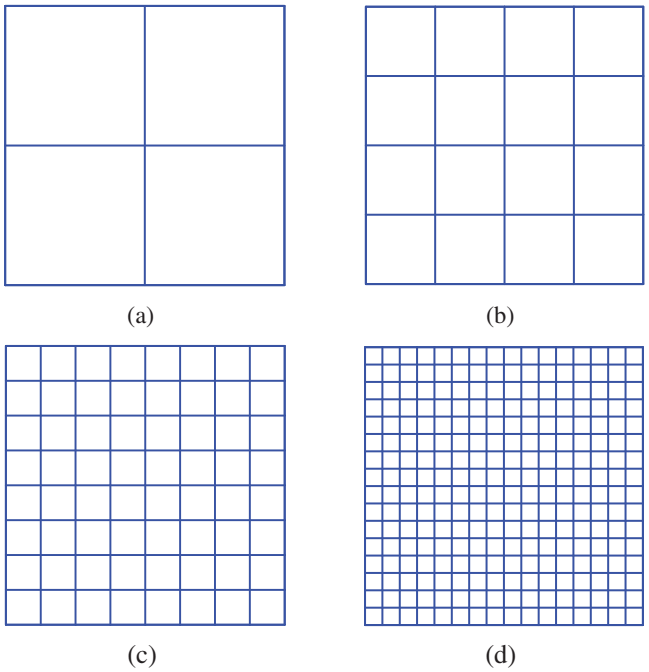

Figure 22: (a) The initial mesh 0 Dofs = 50 the relative error η = 5.5% (b) The mesh 1 Dofs = 98 η = 4.5% (c) The mesh 2 Dofs = 242 η = 3.0% (d) The mesh 3 Dofs = 722 η = 1.5%

meshes in Fig. 22, we can see in Fig. 23 that, adaptive refinement processes apply a reduction of more than 15% in the Dofs at same error level.

Fig. 24 shows the convergence behavior of the displacement ux at point A. The absolute error is defined as $u_x - u_x^{exact}$ where u_x^{exact} is the calculation result of the uniform mesh with 8978 Dofs and u_x is the actual result achieved by the different kinds of meshes. As expected, this example also proves that the adaptive refinement improves the accuracy of the nonlinear isogeometric analysis.

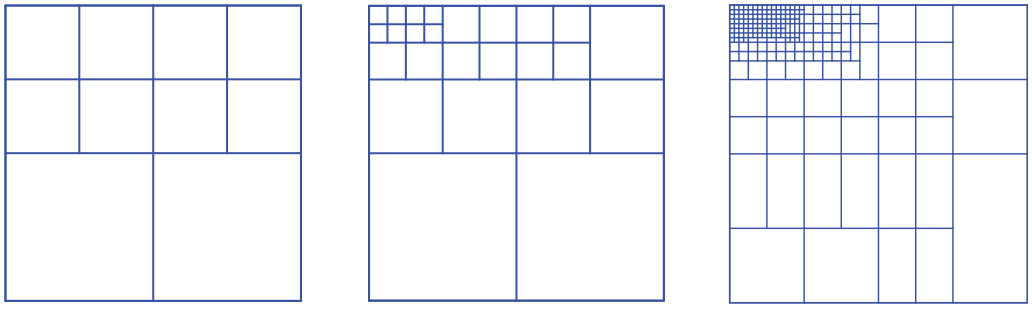

(a) (b) (c)

Figure 23: (a) The t-mesh 1 Dofs = 76 the prescribed error $\bar{\eta}$ = 4.5% (b) The t-mesh 2 Dofs = 200 the prescribed error $\bar{\eta}$ = 3.0% (c) The t-mesh 3 Dofs = 610 the prescribed error $\bar{\eta}$ = 1.5%

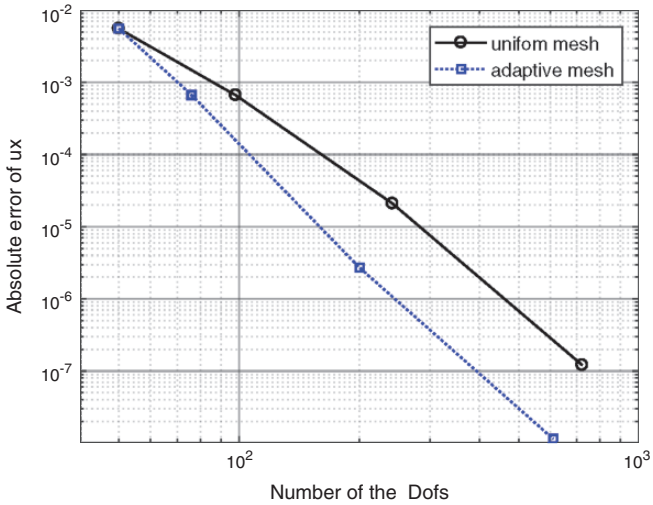

Figure 24: The error of the displacement u_x at point A

6 Conclusions

We have extended the T-spline based isogeometric analysis to the simulation of two-dimensional nonlinear problems, including hyperelasticity and elastoplasticity. We use T-splines to model trimmed designs as one single, watertight geometry, which could be the basis to handle complicated engineering models. Moreover, by combining the error estimate with the local refinement capabilities of T-splines, we provide adaptive refinement meshes during the iteration process of nonlinear analysis. Finally, the obtained results are compared with those from NURBS-based isogeometric analysis and commercial software ABAQUS. The comparison confirm the robustness and accuracy of T-splines in the nonlinear calculation and the advantage in the convergence behavior.

The isogeometric analysis based on T-splines can be a legitimate candidate to simulate nonlinear problems. However, some problems should be scheduled for our future works:

- Among many two-dimensional nonlinear problems, we select hyperelasticity and small deformation elastoplasticity as the research objects, without losing generality. More situations such as the large deformation elastoplasticity and viscoelastoplastic will be conveniently implemented in our framework.

- In our work, the element in which the local refinement parameter is over the prescribed value is refined into new elements. However, in the current analysis framework, we haven't implemented the recovery process, which will be performed if the element's local refinement parameter is under the prescribed value [51].
- The T-spline solids for isogeometric analysis of three-dimensional nonlinear problems will be developed, which allow local refinement and will handle more complex three-dimensional geometry.

Acknowledgement: The authors would like to acknowledge the support by the Natural Science Foundation of China (Project Nos.61972011 and 61572056).

Funding Statement: The work is supported by the Natural Science Foundation of China (Project Nos.61972011 and 61572056).

Conflicts of Interest: The authors declare that they have no conflicts of interest to report regarding the present study.

References

1. Cottrell, J. A., Hughes, T. J., Bazilevs, Y. (2009). *Isogeometric analysis: toward integration of CAD and FEA*. John Wiley & Sons, New Jersey.
2. Hsu, M. C., Wang, C., Herrema, A. J., Schillinger, D., Ghoshal, A. et al. (2015). An interactive geometry modeling and parametric design platform for isogeometric analysis. *Computers & Mathematics with Applications, 70(7),* 1481–1500. DOI 10.1016/j.camwa.2015.04.002.
3. Lian, H., Kerfriden, P., Bordas, S. (2017). Shape optimization directly from cad: an isogeometric boundary element approach using t-splines. *Computer Methods in Applied Mechanics and Engineering, 317,* 1–41. DOI 10.1016/j.cma.2016.11.012.
4. Weeger, O., Narayanan, B., Dunn, M. L. (2019). Isogeometric shape optimization of nonlinear, curved 3d beams and beam structures. *Computer Methods in Applied Mechanics and Engineering, 345,* 26–51. DOI 10.1016/j.cma.2018.10.038.
5. Wang, Z. P., Poh, L. H., Dirrenberger, J., Zhu, Y., Forest, S. (2017). Isogeometric shape optimization of smoothed petal auxetic structures via computational periodic homogenization. *Computer Methods in Applied Mechanics and Engineering, 323,* 250–271. DOI 10.1016/j.cma.2017.05.013.
6. Wang, Z. P., Turteltaub, S., Abdalla, M. (2017). Shape optimization and optimal control for transient heat conduction problems using an isogeometric approach. *Computers & Structures, 185,* 59–74. DOI 10.1016/j.compstruc.2017.02.004.
7. Wang, Y., Benson, D. J. (2016). Isogeometric analysis for parameterized lsm-based structural topology optimization. *Computational Mechanics, 57(1),* 19–35. DOI 10.1007/s00466-015-1219-1.
8. Liu, H., Yang, D., Hao, P., Zhu, X. (2018). Isogeometric analysis based topology optimization design with global stress constraint. *Computer Methods in Applied Mechanics and Engineering, 342,* 625–652. DOI 10.1016/j.cma.2018.08.013.
9. Xie, X., Wang, S., Xu, M., Wang, Y. (2018). A new isogeometric topology optimization using moving morphable components based on r-functions and collocation schemes. *Computer Methods in Applied Mechanics and Engineering, 339,* 61–90. DOI 10.1016/j.cma.2018.04.048.
10. Wang, Y., Xu, H., Pasini, D. (2017). Multiscale isogeometric topology optimization for lattice materials. *Computer Methods in Applied Mechanics and Engineering, 316,* 568–585. DOI 10.1016/j.cma.2016.08.015.
11. Seo, Y. D., Kim, H. J., Youn, S. K. (2010). Isogeometric topology optimization using trimmed spline surfaces. *Computer Methods in Applied Mechanics and Engineering, 199(49-52),* 3270–3296. DOI 10.1016/j.cma.2010.06.033.

12. Hou, W., Gai, Y., Zhu, X., Wang, X., Zhao, C. et al. (2017). Explicit isogeometric topology optimization using moving morphable components. *Computer Methods in Applied Mechanics and Engineering, 326,* 694–712. DOI 10.1016/j.cma.2017.08.021.
13. Zhang, W., Li, D., Kang, P., Guo, X., Youn, S. K. (2020). Explicit topology optimization using iga-based moving morphable void (mmv) approach. *Computer Methods in Applied Mechanics and Engineering, 360,* 112685. DOI 10.1016/j.cma.2019.112685.
14. De Lorenzis, L., Temizer, I., Wriggers, P., Zavarise, G. (2011). A large deformation frictional contact formulation using nurbs-based isogeometric analysis. *International Journal for Numerical Methods in Engineering, 87(13),* 1278–1300.
15. Corbett, C. J., Sauer, R. A. (2014). NURBS-enriched contact finite elements. *Computer Methods in Applied Mechanics and Engineering, 275,* 55–75. DOI 10.1016/j.cma.2014.02.019.
16. Bazilevs, Y., Hughes, T. (2008). NURBS-based isogeometric analysis for the computation of flows about rotating components. *Computational Mechanics, 43(1),* 143–150. DOI 10.1007/s00466-008-0277-z.
17. Bazilevs, Y., Calo, V., Cottrell, J., Hughes, T., Reali, A. et al. (2007). Variational multiscale residual-based turbulence modeling for large eddy simulation of incompressible flows. *Computer Methods in Applied Mechanics and Engineering, 197(1-4),* 173–201. DOI 10.1016/j.cma.2007.07.016.
18. Bazilevs, Y., Calo, V. M., Hughes, T. J., Zhang, Y. (2008). Isogeometric fluid-structure interaction: theory, algorithms, and computations. *Computational Mechanics, 43(1),* 3–37. DOI 10.1007/s00466-008-0315-x.
19. Verhoosel, C. V., Scott, M. A., Hughes, T. J., De Borst, R. (2011). An isogeometric analysis approach to gradient damage models. *International Journal for Numerical Methods in Engineering, 86(1),* 115–134. DOI 10.1002/nme.3150.
20. Bui, T. Q. (2015). Extended isogeometric dynamic and static fracture analysis for cracks in piezoelectric materials using NURBS. *Computer Methods in Applied Mechanics and Engineering, 295,* 470–509. DOI 10.1016/j.cma.2015.07.005.
21. Bui, T. Q., Hirose, S., Zhang, C., Rabczuk, T., Wu, C. T. et al. (2016). Extended isogeometric analysis for dynamic fracture in multiphase piezoelectric/piezomagnetic composites. *Mechanics of Materials, 97,* 135–163. DOI 10.1016/j.mechmat.2016.03.001.
22. Yu, T., Lai, Y., Yin, S. (2014). Dynamic crack analysis in isotropic/orthotropic media via extended isogeometric analysis. *Mathematical Problems in Engineering, 2014,* 1–11. DOI 10.1155/2014/725795.
23. Elguedj, T., Hughes, T. J. (2014). Isogeometric analysis of nearly incompressible large strain plasticity. *Computer Methods in Applied Mechanics and Engineering, 268,* 388–416. DOI 10.1016/j.cma.2013.09.024.
24. Elguedj, T., Bazilevs, Y., Calo, V. M., Hughes, T. J. (2008). B and f projection methods for nearly incompressible linear and non-linear elasticity and plasticity using higher-order nurbs elements. *Computer Methods in Applied Mechanics and Engineering, 197(33-40),* 2732–2762. DOI 10.1016/j.cma.2008.01.012.
25. Taylor, R. (2011). Isogeometric analysis of nearly incompressible solids. *International Journal for Numerical Methods in Engineering, 87(1-5),* 273–288. DOI 10.1002/nme.3048.
26. Elguedj, T., Bazilevs, Y., Calo, V. M., Hughes, T. J. (2008). F-bar projection method for finite deformation elasticity and plasticity using nurbs based isogeometric analysis. *International Journal of Material Forming, 1(1),* 1091–1094. DOI 10.1007/s12289-008-0209-7.
27. Lai, W., Yu, T., Bui, T. Q., Wang, Z., Curiel-Sosa, J. L. et al. (2017). 3-D elasto-plastic large deformations: IGA simulation by bézier extraction of NURBS. *Advances in Engineering Software, 108,* 68–82. DOI 10.1016/j.advengsoft.2017.02.011.
28. Benson, D., Bazilevs, Y., Hsu, M. C., Hughes, T. (2011). A large deformation, rotation-free, isogeometric shell. *Computer Methods in Applied Mechanics and Engineering, 200(13-16),* 1367–1378. DOI 10.1016/j.cma.2010.12.003.

29. Benson, D., Bazilevs, Y., Hsu, M. C., Hughes, T. (2010). Isogeometric shell analysis: the reissner-mindlin shell. *Computer Methods in Applied Mechanics and Engineering, 199(5-8),* 276–289. DOI 10.1016/j.cma.2009.05.011.
30. Du, X., Zhao, G., Wang, W. (2015). Nitsche method for isogeometric analysis of Reissner-Mindlin plate with non-conforming multi-patches. *Computer Aided Geometric Design, 35,* 121–136. DOI 10.1016/j.cagd.2015.03.005.
31. Zhao, G., Du, X., Wang, W., Liu, B., Fang, H. (2017). Application of isogeometric method to free vibration of Reissner-Mindlin plates with non-conforming multi-patch. *Computer-Aided Design, 82,* 127–139. DOI 10.1016/j.cad.2016.04.006.
32. Du, X., Zhao, G., Wang, W., Fang, H. (2020). Nitsche's method for non-conforming multipatch coupling in hyperelastic isogeometric analysis. *Computational Mechanics, 65(3),* 687–710. DOI 10.1007/s00466-019-01789-x.
33. Sederberg, T. W., Zheng, J., Bakenov, A., Nasri, A. (2003). T-splines and T-NURCCs. *ACM Transactions on Graphics, 22(3),* 477–484. DOI 10.1145/882262.882295.
34. Sederberg, T. W., Finnigan, G. T., Li, X., Lin, H., Ipson, H. (2008). Watertight trimmed NURBS. *ACM Transactions on Graphics, 27(3),* 79. DOI 10.1145/1360612.1360678.
35. Dörfel, M. R., Jüttler, B., Simeon, B. (2010). Adaptive isogeometric analysis by local h-refinement with t-splines. *Computer Methods in Applied Mechanics and Engineering, 199(5-8),* 264–275. DOI 10.1016/j.cma.2008.07.012.
36. Vuong, A. V., Giannelli, C., Jüttler, B., Simeon, B. (2011). A hierarchical approach to adaptive local refinement in isogeometric analysis. *Computer Methods in Applied Mechanics and Engineering, 200(49-52),* 3554–3567. DOI 10.1016/j.cma.2011.09.004.
37. Evans, E., Scott, M., Li, X., Thomas, D. (2015). Hierarchical T-splines: analysis-suitability, bézier extraction, and application as an adaptive basis for isogeometric analysis. *Computer Methods in Applied Mechanics and Engineering, 284,* 1–20. DOI 10.1016/j.cma.2014.05.019.
38. Kuru, G., Verhoosel, C. V., Van der Zee, K. G., van Brummelen, E. H. (2014). Goal-adaptive isogeometric analysis with hierarchical splines. *Computer Methods in Applied Mechanics and Engineering, 270,* 270–292. DOI 10.1016/j.cma.2013.11.026.
39. Sederberg, T. W., Cardon, D. L., Finnigan, G. T., North, N. S., Zheng, J. et al. (2004). T-spline simplification and local refinement. *ACM Transactions on Graphics, 23(3),* 276–283. DOI 10.1145/1015706.1015715.
40. Bazilevs, Y., Calo, V. M., Cottrell, J. A., Evans, J. A., Hughes, T. J. R. et al. (2010). Isogeometric analysis using T-splines. *Computer Methods in Applied Mechanics and Engineering, 199(5-8),* 229–263. DOI 10.1016/j.cma.2009.02.036.
41. Scott, M. A., Li, X., Sederberg, T. W., Hughes, T. J. (2012). Local refinement of analysis-suitable t-splines. *Computer Methods in Applied Mechanics and Engineering, 213,* 206–222. DOI 10.1016/j.cma.2011.11.022.
42. Wei, X., Zhang, Y., Liu, L., Hughes, T. J. (2017). Truncated T-splines: fundamentals and methods. *Computer Methods in Applied Mechanics and Engineering, 316,* 349–372. DOI 10.1016/j.cma.2016.07.020.
43. Borden, M. J., Scott, M. A., Evans, J. A., Hughes, T. J. (2011). Isogeometric finite element data structures based on bézier extraction of NURBS. *International Journal for Numerical Methods in Engineering, 87(1-5),* 15–47. DOI 10.1002/nme.2968.
44. Scott, M. A., Borden, M. J., Verhoosel, C. V., Sederberg, T. W., Hughes, T. J. R. (2011). Isogeometric finite element data structures based on bézier extraction of T-splines. *International Journal for Numerical Methods in Engineering, 88(2),* 126–156. DOI 10.1002/nme.3167.
45. Simo, J. C., Hughes, T. J. (2006), *Computational inelasticity.* vol. 7, Berlin: Springer Science & Business Media.
46. Wriggers, P. (2008). *Nonlinear finite element methods*. Springer Science & Business Media, Berlin.
47. Belytschko, T., Liu, W. K., Moran, B., Elkhodary, K. (2013). *Nonlinear finite elements for continua and structures*. 2nd edition. John Wiley & Sons, New Jersey.
48. Kim, N. H. (2014). *Introduction to nonlinear finite element analysis*. Springer Science & Business Media, Berlin.

49. Benson, D. J. (1989). An efficient, accurate, simple ale method for nonlinear finite element programs. *Computer Methods in Applied Mechanics and Engineering, 72(3),* 305–350. DOI 10.1016/0045-7825(89)90003-0.

50. Silva, R., Landau, L., Ribeiro, F. (2000). Visco-plastic h-adaptive analysis. *Computers & Structures, 78(1-3),* 123–131. DOI 10.1016/S0045-7949(00)00078-X.

51. Nie, J. H., Hopkins, D. A., Chen, Y. T., Hsieh, H. (2010). Development of an object-oriented finite element program with adaptive mesh refinement for multi-physics applications. *Advances in Engineering Software, 41 (4),* 569–579. DOI 10.1016/j.advengsoft.2009.11.004.

52. Zienkiewicz, O. C., Zhu, J. Z. (1987). A simple error estimator and adaptive procedure for practical engineerng analysis. *International Journal for Numerical Methods in Engineering, 24(2),* 337–357. DOI 10.1002/nme.1620240206.

53. Wiberg, N. E., Zeng, L., Li, X. (1992). Error estimation and adaptivity in elastodynamics. *Computer Methods in Applied Mechanics and Engineering, 101(1-3),* 369–395. DOI 10.1016/0045-7825(92)90030-N.

54. Zeng, L. F., Wiberg, N. E. (1992). Spatial mesh adaptation in semidiscrete finite element analysis of linear elastodynamic problems. *Computational Mechanics, 9(5),* 315–332. DOI 10.1007/BF00370012.

55. Zienkiewicz, O., Liu, Y., Huang, G. (1988). Error estimation and adaptivity in flow formulation for forming problems. *International Journal for Numerical Methods in Engineering, 25(1),* 23–42. DOI 10.1002/nme.1620250105.